Ultra-broadband plasmon driving selective photoreforming of methanol under ambient conditions

Nasir Uddin[1#], Zhehao Sun[1,2#], Julien Langley[1], Dr. Haijao Lu[1], Dr. Pengfei Cao[3], Ary Wibowo[4], Dr. Xinmao Yin[5,6], Dr. Chi Sin Tang[6,7], Dr. Hieu T. Nguyen[3], Xinzhe Li[8], Xiaoliang Zhang[9], Marc Heggen[3], Rafal E. Dunin‐Borkowski[3], Andrew T.S. Wee[6], Dr. Nicholas Cox[1], Dr. Haitao Zhao[2*] & Dr. Zongyou Yin[1*]*

[1]*Research School of Chemistry, Australian National University, ACT 2601, Australia*

[2]*Materials Interfaces Center, Shenzhen Institute of Advanced Technology, Chinese Academy of Sciences, Shenzhen 518055, Guangdong, PR China*

[3]*Ernst Ruska-Centre for Microscopy and Spectroscopy with Electrons, Physics of Nanoscale Systems (ER-C-1), Leo-Brandt-Str. 1, 52428 Jülich, Germany*

[4]*Research School of Electrical, Energy and Materials Engineering, Australian National University, ACT 2601, Australia*

[5]*Shanghai Key Laboratory of High Temperature Superconductors, Physics Department, Shanghai University, Shanghai, 200444, China*

[6]*Department of Physics, Faculty of Science, National University of Singapore, Singapore 117542, Singapore*

[7]*Institute of Materials Research and Engineering, A□STAR (Agency for Science, Technology and Research), Singapore, 138634, Singapore*

[8]*Department of Materials Science and Engineering, National University of Singapore, Singapore 117574, Singapore*

[9]*Institute of Energy and Environmental Engineering, School of Energy and Power Engineering, Dalian University of Technology, Dalian 116024, PR China*

#: These authors contributed equally to this work

[*]*Corresponding authors. Email: p.cao@fz-juelich.de; ht.zhao@siat.ac.cn; zongyou.yin@anu.edu.au*

Abstract

Liquid methanol (CH_3OH) is considered as potential hydrogen (H_2) energy carrier storage medium that has scientific and industrial importance, requiring technological processes to extract CO_x free molecular H_2 from effectively given that highly stable and active catalytic materials mediate such processes. Existing processes have been made acceptable progress by employing in-housed built various catalytic materials, for example, electrocatalysts and photocatalysts, yet lack of complete CO_2 abatement from reaction environment. Here we take this opportunity to integrate Cu nanoplasmon with WC/W nanoparticles (NPs) and found that the photocatalytic H_2 efficiency from pure liquid CH_3OH was exceeded by almost 14 folds (2176.66 to 156.83 $\mu mole.g^{-1}.h^{-1}$) in comparison to its counterparts under solar light illumination. Collectively, the plasmonic photocatalytic activities were sustained for more than 41 days from six successive tests avoiding the formation of CO_x compounds in the reaction. The formation of energy intensive chemical products from CH_3OH corroborate the very selective reaction pathway. We demonstrate strain mediated catalytic activity of WC NPs and those activities can be promotional when nanoplasmonic Cu interact that dictates the reaction dynamics. Complementary theoretical assessments unfold that the broadband absorption from plasmonic Cu NPs generates local electric field to perturbate reaction microenvironment at interfacial WC surface, those redistribute the stored energy to nearest CH_3OH molecules, resulting in self-separable H_2 and preferential products formation. We illustrate that the integration between traditional plasmonic Cu NPs and relatively unknown plasmonic WC NPs would be a new paradigm in plasmonic photocatalysis that possess many unique characteristics which might not be achievable over existing traditional catalytic materials.

1. Introduction

Methanol has been recognized as a good H_2 storage medium for the greener H_2 economy gradually moving away from fossil fuel, as methanol possesses several unique merits: absence

of strong C-C bonds facilitating reforming at mild conditions, room temperature (RT) liquid phase enabling transportation via existing gasoline/oil infrastructures, and relatively high gravimetric hydrogen content (12.6%). Hydrogen production from pure methanol (CH_3OH) under solar light is a promising pathway as opposed to water splitting which suffers from the chronic photochemical instability issue even from noble-metal based photocatalysts (Supplementary Table S1) [1, 2]. Intensive research has been conducted for the latter method while few reported the viable utility of the first one. Many obstacles towards its practical realization at a large scale remains to be prioritized whilst the development of active and durable catalyst materials for hydrogen production from ambient CH_3OH splitting is among the uttermost important ones. In this perspective, the search for non-precious metal based alternatives is crucial and much demanding. Among many potential catalytic materials, there are very limited materials presence that can concurrently meet the activity and stability specifications [3]. Early transition metal carbides (TMCs) have been viewed as sustainable non-noble metal catalysts for H_2 generation owing to their ubiquitous abundance, low cost, high chemical stability and excellent catalytic activities towards range of reactions such as dehydrogenation [4], hydrogenation [5], methane to syngas [6], and ammonia decomposition [7].

One prospective TMC material is tungsten carbide (WC) which shows great potential in chemical transformations. Recent demonstrations highlights that WC materials possess visible to near infrared (NIR) light absorption ability, suggesting it could have localized surface plasmon resonance (LSPR) feature [8]. As generally understood that LSPR is a collective oscillation of the free electrons in the metal nanoparticles when visible light interaction occur [9]. Arguably, such excitation of LSPR is often creditable to noble metals (Pt, Au, Ag) [10-12] nanostructure which indirectly discourage the utilization of noble free plasmonic metals as photocatalytic materials for chemical reaction. Conversely, a rich set of studies advocates far

better LSPR excitation on noble free plasmonic nanostructures which mediates appreciable excited charge carriers under visible light illumination, for example, Al [13], Mg [10], Cu [14]. Unquestionably, metallic Cu nanoparticles (NPs) may positively overwhelm others, has been recognized as plasmonic photocatalysts in performing electron-transfer reactions at the nanoparticle and the reacting molecules interface, resulting highly selective and improved catalytic performance [14-16]. Adhering to improve photocatalytic efficiency, plasmonic Cu NPs is traditionally hybridized with other metals and/or metal oxide, forming bi-metallic alloy or metal-oxide nanoplasmonic heterostructures to functionalize the excited charge carriers in achieving preferential products over undesired ones from the reaction. While remarkable plasmonic photocatalytic performance is reassured over Cu NPs, the thermodynamic easiness of surface oxidation leading to strongly damped LSPR, resulting compromised stability and reactivity. In this context, we conceptualized the fabrication of unconventional hybrid plasmonic nanostructure between Cu NPs and WC/W materials such that it would ensure sustained and selective reaction via LSPR excitation upon light illumination, affording substantial enhanced photocatalytic activities.

We hypothesized that the tailored non-traditional nanoplasmonic hybrid structure would have manifolds features: (1) because of the large immiscibility gap between Cu and W metal, the formed plasmonic nanocomposite could possess unique functionalities those are expected to convey high catalytic activities at nanointerface, (2) formation of cooperative and reactive strain effect from core W to shell WC structure in the composite would lower the reaction height significantly under plasmonic excitation, (3) absorption of broad solar spectrum by Cu NPs that can generate more hot charged carriers (hot e^- - hot h^+ pairs) to WC surface and the local electromagnetic field enhancement [17] at the LSPR wavelengths of Cu NPs, and (4) formation of protection scheme around Cu NPs which is yet crucial to heighten the catalysts stability under working conditions. Indeed, the protection scheme would permit quicker charge

carrier diffusion and reaction intermediates species absorption at nanohybrid interface [18], resulting higher photocatalytic performance. However, these in-situ prepared materials would be the resemblance of the engineering of plasmon and strain induced catalytic functions within single materials which can mediate high yield H_2 activities from pure CH_3OH under solar light irradiance. This opens new physical insights about the reaction selectivity and dynamics at the nanointerface relying on the proper choice of the light excitation characteristics. We deduced that at visible light frequency or wavelength, the plasmonic excitation would effectively transfer the energy between the constituting metal parts in the composite, resulting substantial increment in photoactivity and modulating the product formation in liquid CH_3OH conversion.

By taking the above beneficial traits, here we design a unrivalled plasmonic nanohybrid structure of Cu-WC/W NPs where W and WC works as core-shell NPs adopting a solid state synthesis under hydrogen vacuum atmosphere at 850 °C. Importantly, measurable steps were taken to prevent excessive surface carbon-a known issue when synthetic route deal with carbide formation [19, 20]. Favourably, we achieved nanscale structures of WC alongside of in-situ produced metallic W that could form disruptive heterointerfaces resulting in higher electronic conductivity and more catalytic active sites [21]. Combining both experimental and theoretical studies, it is however, observed that plasmon excited charge carrier preferentially flows from Cu NPs to catalytic active W-WC core-shell sites under solar light illumination maintain highly achievable photocatalytic performance. Further demonstration on enhanced photocatalytic performance of plasmonic Cu-WC/W NPs unfolds that pure CH_3OH decomposition could form H_2 avoiding CO_x free products generation suggesting very selective and long-standing strained mediate catalytic activities at nanointerface. Admittedly, these plasmonic metallic nanohybrid structure would behave quite differently from traditional plasmonic nanostructures in the context of LSPR excitation that regulates the energy of excited charge carriers for CH_3OH dissociation. Nevertheless, these nanohybrid structure would become a new family of

plasmonic photocatalysts for pure CH_3OH decomposition reactions upon solar illumination that yet to be reported.

Liquid CH_3OH decomposition reaction into H_2 by plasmonic Cu-WC/W NPs under solar light illumination has deep-rooted impacts towards so-called methanol economy. Achieving sustainable methanol economy has industrial relevance while there are few technical issues remained that needs to be addressed follows: (1) the H_2 production should be highly stable without forming toxic products or greenhouse gases, indicating the catalytic materials must be intrinsically active and effectively offer long-standing performance [22, 23]. Earlier studies have been emphasized on improved catalytic performance whereas lesser control over toxic compounds formation outweigh their catalytic effectiveness [24-26]. And (2) the storage and transportation of hydrogen has to be done in a safer way and support cheaper supply chain infrastructures. An elegant way to transport and store hydrogen in liquids and yields in-situ hydrogen over catalytic materials which play role on chemical bonds dissociation [22, 23]. Rich chemistry and simple atomic structure makes CH_3OH as a promising hydrogen carrier in this regard while it plays roles on the carbon cycle closure (scheme 1). We postulated that the integration of uncommon plasmonic nanohybrid structure would overcome these obstacles considerably because the cooperative effects between the plasmonic excitation and the catalytic active sites. We reasoned multifaceted advantages of Cu-WC/W NPs towards H_2 economy that cannot be achievable by traditional plasmonic photocatalysts: (1) experimentally deployment of pure CH_3OH liquid solution for in-situ H_2 production at room temperature without adding any sort of reactive reagents and/or promoters [2], (2) utilization of naturally available and inexpensive solar energy to induce the photoredox reaction, (3) produced H_2 completely free from CO_x compounds, and (3) preferential formation of various value added multi-carbon based liquid chemicals. Notably, the hybridization between traditional plasmonic Cu NPs and relatively unknown WC NPs in plasmonic photocatalysis would guide us on the mechanistic

understandings of CH_3OH reaction and its selective behaviours towards industrially important target product formation under solar light excitation. Such unconventional plasmonic nanohybrid structure would add further knowledge in plasmon-mediated solar fuel generations and will encourage to fabricate more robust plasmonic materials that would work very differently than available ones.

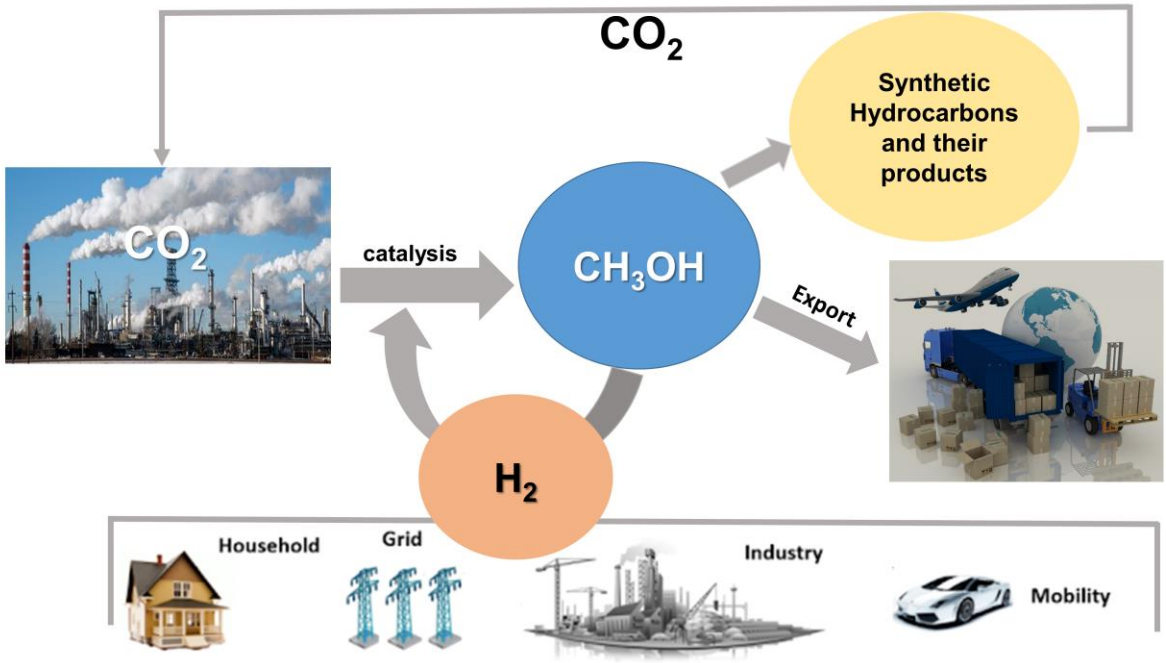

Scheme 1 | A closed loop carbon cycle under methanol economy starting from CO_2 feedstock to product liquid methanol to H_2 and other industrial products has potential to achieve carbon neutrality.

2. Experimental

2.1. Chemicals

Urea (ACS reagent, 99%), copper (II) chloride ($CuCl_2$, 97%), tungstic acid (H_2WO_4, 99%), alcohols such as methanol (HPLC grade, 99.9%), ethanol (HPLC grade, 99.5%), methylal ($C_3H_8O_2$, 99%), methyl formate ($C_2H_4O_2$, 99%), and free radical spin trapping reagent 5, 5-

Dimethyl-1-pyrroline N-oxide (DMPO, 97%) were all purchased from Sigma Aldrich. Pure H_2 (99.999%), and Ar (99.997%) were purchased from BOC gas, Australia.

2.2. Catalysts Preparation

A simple procedure was followed to synthesize the Cu-WC/W plasmonic nanoparticles with varying loading conditions. Initially, we have mixed up urea and tungstic acid precursor in 2 mL ethanol solution keeping total weight not to exceed 2.0 grams. Later, we have added desired amount of noble free Cu precursor into the above mixture. After this, we stirred the mixture for couple of hours and aged the mixture for whole nights following 3 hours annealing in 850 ^{o}C under H_2 vacuum atmosphere. Once the annealing process was done, then we did the passivation of the materials until the CVD temperature reach to room temperature. The prepared materials was used without any further treatment. Unless otherwise stated, very identical synthetic approach was used to prepare other samples in this work.

2.3. Catalysts Characterization

Aberration-corrected (Cs corrector) high-resolution TEM experiments were performed on an FEI Titan 80–300 microscope at 300kV, which was equipped with a 2k × 2k Gatan UltraScan 1000 CCD camera. HAADF STEM imaging and EDX mapping analysis were conducted using a Hitachi HF5000 at 200kv, which is a cold FEG TEM/STEM with a Cs probe corrector equipped with double EDX Ultra 100 detector from Oxford Instruments. Scanning electron microscopy (SEM) samples were prepared by sonication of powder/ethanol mixture and then drying the suspensions onto silica substrate. Sample analysis was performed by using a field-emission SEM (ZEISS Sigma 300) operated at 5.0 kV. Ultraviolet-Diffuse reflectance spectrophotometer (UV-DRS) measurement was conducted on Lamda 465 (Serial No: 465K7121104, PerkinElmer) instrument. A blank without sample was measured as background before testing the samples. Powder X-ray diffraction (XRD) measurement was done on a

PANalytical Empyrean using Cu Kα (λ=1.5406 Å) radiation with a generator voltage and current of 45 kV and 40 mA, respectively. X-ray photoelectron spectroscopy (XPS) was performed on a Nexsa (ThermoFisher Scientific) spectrometer. The system work function was calibrated for each sample by setting the main line of the C 1s spectrum to 284.8 eV. Each high resolution spectrum was fitted with a Gaussian-Lorentzian (70%-30%) line shape using a Shirley background. Electron paramagnetic resonance (EPR) measurement was done on a commercial Bruker E500 spectrometer equipped with an ER4122 SHQ resonator with the following parameters: 150 mW, 9.8 GHz light and 0.5 G modulation amplitude. Liquid solution EPR measurements were analysed using a quartz flat cell. For spin trap experiments, certain amount of photocatalytic samples was dispersed in 10 mL methanol, followed by solar illumination for 2 hours at room temperature. A small volume of the illuminated solution was then mixed with a certain volume of DMPO aqueous solution (150 mM). The reaction mixture was then used for EPR measurement. For reference purpose, an aliquot of this mixture was taken prior to illumination and its EPR spectrum was recorded. Time dependent in-situ EPR measurement was done in the similar way as just mentioned except that the sample with DMPO trapper illuminated directly focused on the centre of the EPR cavity where the quartz flat cell located and acquired the spectrum at certain time interval. X-ray absorption near-edge structure (XANES) experiments were done at the National Synchrotron Radiation Research Center (NSRRC), Hsinchu, Taiwan. Cu K-edge spectrum were acquired at Wiggler beamline 17C and 07A using a Lytle cell or transmission cell. A double crystal Si (111) monochromator was used with an energy resolution $\Delta E/E$ better than 2×10^{-4}. At Cu-K edge, the energy resolutions were about in the range of 8770 to 9840 eV. The focused beam size at the sample position was 4 mm × 2 mm. Athena software [27] was utilized to process and analyse the raw XAS data including background removal, edge-step normalization, and Fourier transform. Artemis software [27] was used to fit the Fourier transformed EXAFS data with a model. The normalized $\chi(E)$ was

transformed from energy space to k-space using Artemis software. The k^2-weighted $\chi(k)$ data in the k-space ranging from 3.0 to 10.5 $Å^{-1}$ at Cu K-edge, was Fourier transformed (FT) to r-space to isolate the EXAFS contributions from different coordination shells. The fitting of EXAFS data was done for only Cu-Cu first shell in r-space ranging from 1 to 3.0 Å by using a nonlinear least squares algorithm. Phases and amplitudes have been calculated by FEFF8 code using the Artemis software [27]. A conventional three-electrode system was used to measure electrochemical impedance, in which saturated Ag/AgCl electrode, Pt wire and glassy carbon electrode (diameter~ 3mm) with photocatalysts (loading density ~ 0.28 $mg.cm^{-2}$) act as reference, counter and working electrodes, respectively. Electrical signal from above electrode system was processed by PARSTAT 3000 station with 1.2 kHz frequency at a constant voltage of 1.0 V against Ag/AgCl scale. Photocurrent measurement was performed using the same instrumentations above in which the solar light switching on and off condition was controlled manually keeping the elapsed time interval identical. Wavelength dependent photocurrent measurement was done by varying the filter to 420, 700, and 800 nm whereas control experiment was done at AM 1.5 G solar illuminated conditions. All these experiments were performed in pure CH_3OH solution using 0.1 M KOH electrolyte at 1.0 volts in the scale of Ag/AgCl. Time resolved photoluminescence (TRPL) curves were captured at room temperature using an Horiba iHR 320 mm spectrophotometer equipped with a compact single-photon silicon detector (PPD-900, detection range between 350-920nm). A 485-nm picosecond pulse laser (Horiba DeltaDiode) was used as an excitation source with a pulse width of 80 ps. The laser light was focused on the S1-S5 samples through an Olympus BX53 microscope equipped with a 50x objective lens and an X-Y micro-positioner. All measurements were done with a 1 MHz repetition rate with 800 ns time range. The lifetimes were calculated by fitting the decay curves and instrument function response with a bi-exponential decay function. Nuclear magnetic resonance (NMR) spectroscopy was done on Bruker 400 MHz instrument

keeping the ratio of sample to deuterated methanol (CD_3OD) at 4:3 to identify the ^1H species before and after reaction.

2.4. Photocatalytic Experiment

Photocatalytic methanol decomposition reactions were performed in a 15 mL quartz bottle at ambient working conditions. Atop of the bottle, a silicone rubber septum (diameter ~ 13 mm, thickness ~3 mm, Specialty Silicone Products, Inc., U.S.A) was fixed to contain the gaseous products from reactions. A 300 W Xenon lamp source (Microsolar300, Beijing Perfectlight Technology Co., Ltd, China) with AM 1.5 G filter was horizontally placed to concentrate the light on the reaction solution. Filters were changed to do other similar experiments where needed. Depending on the type of experiments, a desired amount of photocatalyst was added into the reactor while 90 min sonication was performed to disperse the photocatalysts in 10 mL CH_3OH solution. To remove any residual air contamination from reactor bottle, the degassing was done using Ar at least for an half hour. Gas chromatography, GC, (Nexis 2030, Shimadzu Scientific instruments) was utilized to detect gaseous products from the reaction which housed with a thermal conductivity detector (TCD), and a flame ionization detector (FID) and a ShinCarbon (100/120, 1mm ID, 1/16″ OD) column. Using 100 μL Hamilton syringe (Hamilton company Inc, U.S.A), 50 μL of gaseous species from the empty space of the reactor bottle was injected in GC before illuminated the light which works as reference point. Next, we followed the similar approach to inject the formed gaseous products after illumination and record the peak area (PA) from GC. A standard calibration curve of pure hydrogen was utilized to quantify the formed gaseous products. Duration of each photocatalytic test relied on the type of experiments, for example, the stability test was continued for several days whereas the catalyst screening test last typically for 120 minutes. Liquid products identification after illumination was done on Agilent 7890 A GC housed with a FID and 7010 Triple Quadruple GC/MS/MS with helium as carrier gas. Injections were split in 100:1 with a split flow of 150 mL/min and

delivered through an autosampler. The inlet temperature was 220 ºC, while oven temperature was set in the range of 40-240 ºC, among which a ramping rate of 5 ºC/min was applied in the range of 40-100 ºC with no hold time and another ramping rate of 20 ºC/min used in the range of 100-240 ºC with a hole time of 3.5 min. Scans were measured from 10 mass to 300 mass using 300 ms scan time. The FID temperature was set to 250 ºC and the injection volume was 1 µL. To match and authenticate the formed liquid products after reaction, National Institute of Standards and Technology (NIST), U.S.A, MS spectral Library was utilized.

3. Results and Discussion

Changing in electron distribution by adopting carbon molecules in its structure, the metallic tungsten can be tuned to tungsten carbide (WC) which deemed to be effective for many chemical reactions as does noble-metal Pt [28]. Attempts have been made to test this hypothesis in recent years, especially for H_2 evolution reaction [8, 29] while its utilization as plasmonic materials with noble free metallic Cu will be an additional steps in advancing current understandings in photocatalytic as well as materials science fields. We take this opportunity to prepare unconventional plasmonic Cu-WC/W nanostructure using carburization process at high temperature under vacuum hydrogen atmosphere (Note S1). By varying the weighted amount of Cu precursor, we prepared in-situ 1, 2, and 4 wt% Cu-WC/W materials while the control WC/W sample followed the similar procedure. Among the in-situ prepared Cu-WC/W samples, we noticed that 2% Cu-WC/W unveils remarkable catalytic efficiency from pure CH_3OH splitting into H_2 within this work (Figure S1). Additionally, we practiced this synthetic route to make a rich catalogue of other non-noble metallic catalytic materials such as Ni, Mg, Ca, and Zr, which, however, showed negligible catalytic performance as compared with 2% Cu-WC/W sample (Figure S2). Furthermore, the wavelength dependent studies confirmed that the working illumination energy will be AM 1.5 G simulated solar light, which covers entire visible spectra (Figure S3).

Figure S4 shows the X-ray diffraction (XRD) pattern for in-situ prepared WC/W sample assignable to elemental W having the body–centered cubic (bcc) structure with multiple peaks at 2θ = 40.35, 58.37, and 73.35°, corresponding to (011), (002), and (112) plane, respectively (ICSD # 653433); whereas WC shows no visible peaks implying that WC might have crystalline solids with short-range order. After introduction of bare Cu precursor, the XRD pattern of WC/W exhibited three additional peaks, maintaining the peaks related to WC/W while three peaks could be assigned to the (111), (002), and (022) planes of face-centered cubic (fcc) elemental Cu phases located at 2θ = 43.52, 50.56, and 74.28°, respectively [30, 31]. No other peaks were identified, indicating that the in-situ synthesized WC/W nanoparticles (NPs) is free from any other impurities. Traditionally, when carbides material prepared in hydrogen reduction atmosphere at above 800 °C in presence of excessive gaseous carbon precursors, there is a possibility of coke formation on WC surface which can be detrimental towards catalytic activity [19, 32]. Nevertheless, the synthetic approach within this study is selectively engineered by limiting the carbon precursor volume which permits to form only WC besides elemental W and thus avoiding coking formation.

Aberration-corrected high-resolution TEM study reveal that the in-situ prepared WC/W NPs have average particle size ~56 nm (Figure S5) as shown in Figure 1a, b. Representative W component (Figure 1c) shows that W has lattice spacing about 0.22 nm and primarily formed in [111] direction (Figure 1d) whereas WC marked with 0.18 nm of interplanar distance and regulated in [110] direction (Figure 1e, f). We also noticed that WC NPs may have some lattice distortion, which could be associated with the presence of W atoms inducing strain by the atomic lattice mismatch as shown in Figure 1e and fast Fourier transform analysis (Figure 1f). Note that the formed WC nanostructure is dominated by small crystal domains with slight amorphousity, which is well align with XRD results. Observing from TEM image, it was disclosed that the metallic W formed as core while WC as a shell. Figure 1g shows TEM image

of optimized 2% Cu-WC/W sample in this work which highlights shape-scattered particles, having average size ~45 nm (Figure S6), whereas Cu particles on the surface of WC layer as shown in Figure 1h, corresponding an average 4-6 nm size distribution profile (Figure S7), which is comparable with purely prepared Cu NPs size (Figure S8). Magnified TEM shows that the composite consists of WC, W, and Cu whereas Cu NPs possess lattice spacing of 0.21 nm and its zone axis was indexed along [011] direction (Figure 1i and inset FFT image). Closer inspection of Figure 1h and 1i reveals that Cu NPs was primarily formed at the shell side of WC, not at the core W side due to the immiscibility of Cu with elemental W [33, 34]. Figure 1j shows the HAADF images of 2% Cu-WC/W sample which unveils the epitaxial growth of WC components on W. It is suggested that the carbide formation in presence of carbon under reducing agents like H_2 gas can mediate in-situ heteroepitaxial growth at high temperatures [35]. The epitaxial growth of WC and W in the gas phase deposition could be originated to the lattice mismatch, resulting the formation of hybrid core-shell nanostructure. Depending on the degree of lattice misfit, the resulting interface between two materials can be coherent to non-coherent [36, 37]. High-angle annular dark-field transmission electron microscopy (HAADF-TEM) shows the epitaxial orientation of the core and shell and its corresponding interface (Figure 1j). Figure 1k (green rectangle box) reveals the epitaxial growth boundary between WC and W whereas a semicoherent growth of WC on the d {011} =0.22 nm plane of pure W is shown in green direction (Figure 1l). Because the WC layer is thin and at the surface of W, lattice distortion occurs. As a result, the lattice distance of epitaxial formed WC in {110} is expanded to 0.25 nm. By using formula of {d(WC)-d(W)}/d(W), the misfit along the plane {110} is 12% for WC layer. Similarly, during the epitaxial growth along with W d {101} = 0.22 nm plane (yellow direction in Figure 1l), the lattice distance of WC expanded from 0.22 to 0.28, and then the {001} plane formed. The lattice misfit in the later case is about 21%, which implies that WC might have large lattice volume. Different than this study, a core Au

and shell CdS nanostructure up to 43% lattice misfit was reported previously [36]. Furthermore, the resolved TEM image (Figure 1m) and FFT analysis of WC particles (Figure 1n) unveils the observable single diffraction peak in [110] direction of WC, which highlights the compressive strain from W. Moreover, the representative W in the composite exhibits similar diffraction data (Figure 1o, p) as observed for WC, confirming the semi-coherently strained epitaxial overgrowth, resulting the formation of core-shell nanohybrid structure. In addition, STEM-EDX elemental mapping unfolds the co-existence of W, C and Cu (Figure 1q-u) in the composite whereas the bare WC/W sample exhibits the presence of W and C (Figure S9).

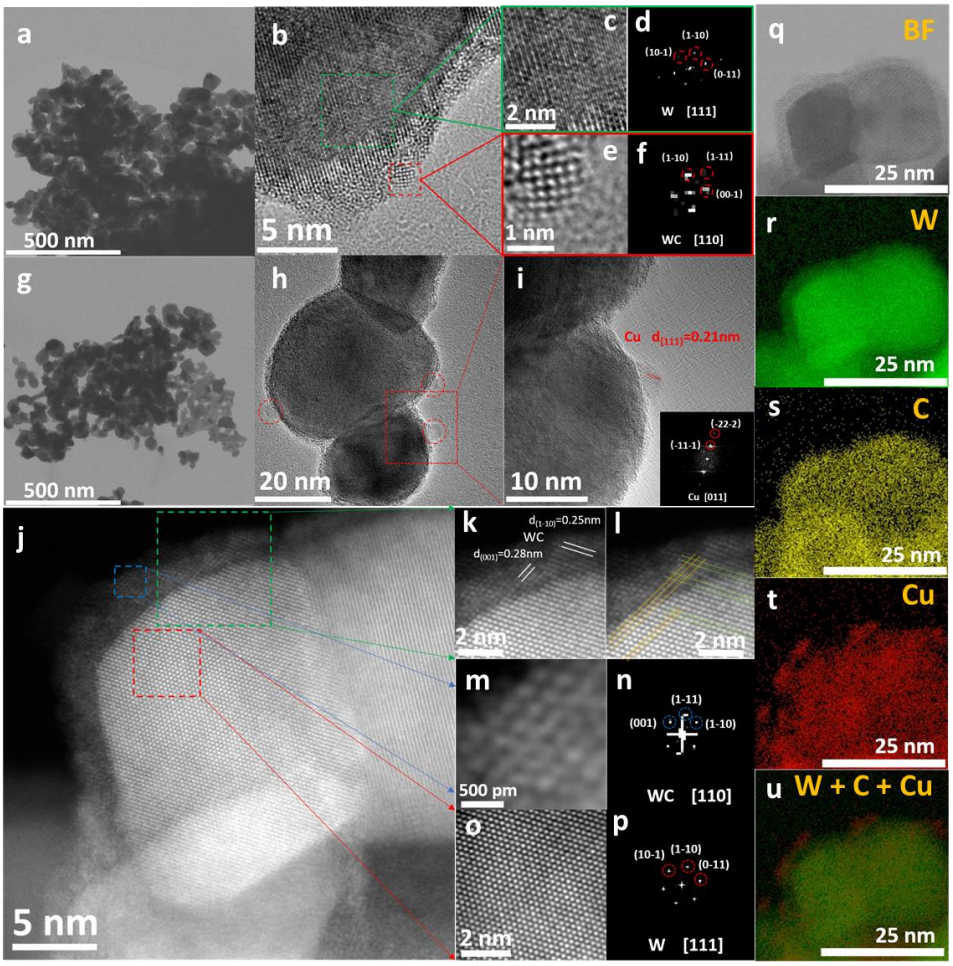

Fig. 1 | Catalyst characterization. (a) TEM image of WC/W sample in low magnification; (b) TEM image of WC/W sample with high resolution; (c) representative W component; (d) the corresponding FFT pattern of W; (e) representative crystalline WC; (f) the corresponding FFT pattern of WC; (g) TEM image of 2% Cu-WC/W sample in low magnification; (h) Cu particles with different particle size stand on the surface of WC layer; (i) TEM image of representative Cu particle in high magnification, and the insert image is the corresponding FFT pattern; (j) HAADF images of Cu-WC/W sample; (k) cropped area near the epitaxial boundary of W and WC components; (l) the epitaxial relationship between W and WC; (m) representative WC particles; (n) the corresponding FFT pattern of W; (o) representative W component; (p) the

corresponding FFT pattern of W. (q) – (u) Bright Field (BF) image of 2% Cu-WC/W sample and EDX maps of W, C, Cu and W+C+Cu.

Above microscopic results corroborated that the in-situ formed core W and shell WC adopts Cu NPs in the structure. This core-shell geometry is very promising to expedite the bond-breaking and bond-making reactions, however, the structural and catalytic stabilities of this materials may encounter oxidation event at room conditions [38]. Such unwanted events may lead to more complex scenarios, especially with Cu NPs presence [39], possibly changes the structure of as-prepared Cu-WC/W samples. We infer that during the carburization process at above 850 ℃, a part of the solid carbon diffuse to Cu region and protects it from not being oxidized or corroded upon air exposure and thus increase its stability, which was verified from TEM study (Figure1, and Figure S8) [18]. Weakened miscibility between W and Cu NPs could be the reason to facilitate carbon diffusion towards Cu region under the reduction environment. As a result, the carbon coverage on top of Cu NPs well maintained Cu's stoichiometric and electronic structures, and hence its functionalities. To verify this inference, x-ray photoelectron spectroscopy (XPS), X-ray absorption near edge structure (XANES) and extended X-ray absorption fine structure spectroscopy (EXAFS) were performed. Figure 2 a, b shows fine W 4f spectrums with and without Cu addition, which can be fitted into multiple peaks in the range of 30 to 40 eV, indicating the mixed chemical oxidation states of the W atom. The peaks located at binding energies of 31.46 (W $4f_{7/2}$) and 33.67 eV (W $4f_{5/2}$) are assigned to the metallic W while the peaks at 31.88 and 34.10 eV corresponds to W–C bond (WC) [32, 40] and those at higher binding energies of 36.04 (W $4f_{7/2}$) and 38.07 eV (W $4f_{5/2}$) are attributed to unavoidable surface oxidation state of tungsten carbide when the samples were exposed to air [21, 32, 41, 42]. Furthermore, C 1s spectrum before and after Cu introduction revealed the similar atomic composition in the nanohybrids (Figure S10). High-resolution XPS profile of Cu 2p region (Figure 2c) exhibits two main peaks at 932.57 and 952.37 eV in a 2:1 area ratio, representing

the electron splitting energies of Cu $2p_{3/2}$ and Cu $2p_{1/2}$, respectively, which is a typical feature for Cu^0 state [43, 44]. The absence of shake-up satellites feature between 940-945 eV [45] and other characteristics peaks ascribed with Cu^{2+} for Cu $2p_{3/2}$ and Cu $2p_{1/2}$ were not identified at around 942.2 and 962.0 eV [46], indicating that there is no Cu^{2+} species formed. As observed in Figure 2d that an intense peak located at 8992.95 eV corresponds to so-called white-line peak, signalling a greater number of coordination number in the first shell of the cation along with more uniform bond length distribution [47]. The peaks at 8980.03 eV is the representative of Cu^{II} state [48], which is due to the 1 s → 4p electronic transition. Other electronic transitions such as 1 s → 3d (pre-edge peak) for Cu^{II} state, and 1 s → 4p (rising-edge peak) for Cu^{I} state were not observed [47]. The Fourier transform (FT) of the Cu-K edge with fitted data is represented in Figure 2e to highlight the local structure of Cu at the atomic scale. An intense peak was remarked at R< 2.81 Å, whereas the absence of well-defined features at R > 2.81 Å is corroborating to the large structural disorder beyond the first-shell surrounding the central atom (Figure 2f) [49]. This effective radial distribution strongly suggest that under H_2 annealing at 850 ºC, the copper species fully reduced to metallic Cu^o without any Cu-O formation [50]. By further performing quantitative EXAFS analyses, we estimate an average Cu-Cu bond length of 2.41 Å while the coordination number is 12 which is in good agreement [51] with fcc structure Cu elements which thus confirmed that Cu has no other bonded network in the nanohybrid. Therefore, above XPS, XANES, and EXAFS analysis further supported the formation of plasmonic hybrids with metallic Cu NPs anchored onto the WC/W nano templates.

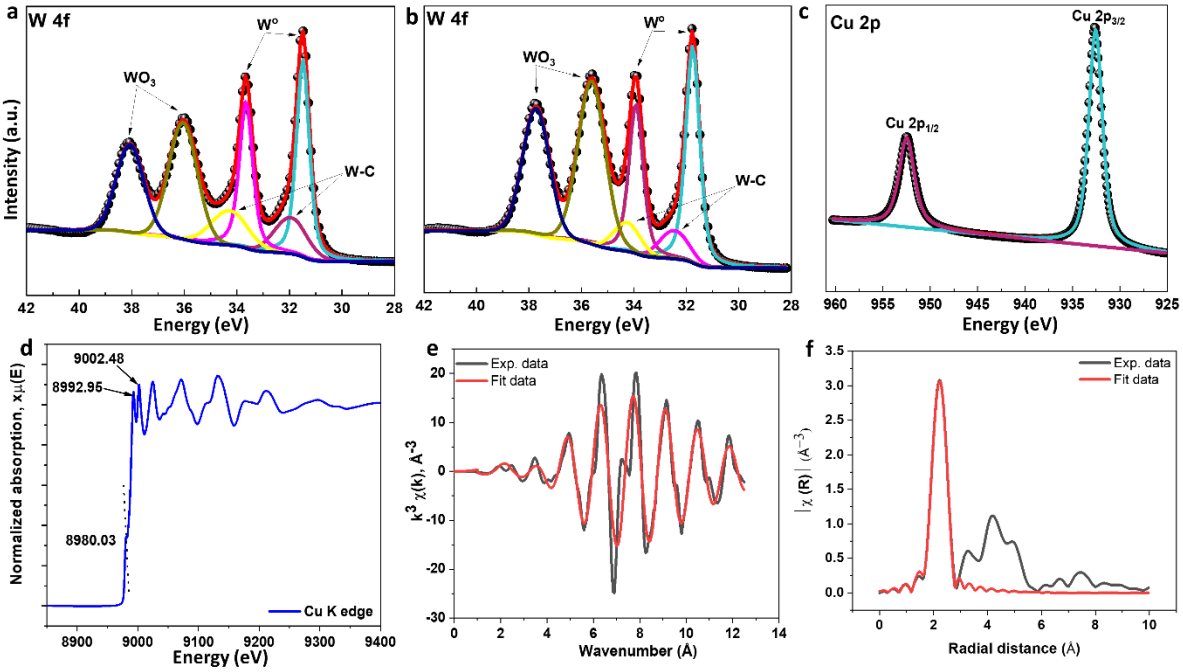

Fig. 2 |. XPS and XANES of plasmonic 2% Cu-W/WC catalysts. (a, and b) XPS profile for W4f states before and after introducing Cu, (c) XPS profile for Cu 2p states. Synchroton chracterization of plasmonic 2% Cu-W/WC catalysts. (d) Normalized Cu K-edge XANES spectra, (e) k^3-weighted FT EXAFS spectra obtained in the range of 3-10.55 $Å^{-1}$, and (f) Magnitude of the Fourier transform (FT) of k^3 $\chi(k)$ in the R space. Fitting was done only for first shell.

The multi-components plasmonic photocatalysts are potential candidates to tailor solar harvesting features, photoexcited charge carriers migration across the nano-heterointerface, the LSPR and the strain field, which are adaptable for tailoring photoacativity [52, 53]. In this perspective, the development of highly stable plasmonic Cu-based NPs along with metallic WC/W core-shell structure as just demonstrated above is a far-reaching step towards utilizing full solar spectrum due to their broad LSPR covering from the UV to the visible and to near infrared region. Hydrogen formation from pure CH_3OH dehydrogenation at ambient conditions is believed to be interlinked with the utilization of plasmonic excitation and amlification of hot carriers to catalytic sites. Excitation of LSPR of the 2% Cu-WC/W nanohybrids gives rise to

strong optical absorption, scattering, and electromagnetic field confinement while the decay of LSPRs into hot carriers and their migration and diffusion into specific adsorbates accelerate the targeted reaction. The illumination of a metallic nanohybrids begins the process to harvesting hot charge carriers as well as their energy distribution to the WC sites which primarily depends on NPs geometry configuration. Therefore, the plasmonic catalytic activity of 2% Cu-WC/W NPs is closely related to its structural dimension that can harvest full solar spectrum with active reaction sites [53, 54]. To deepen the knowledge on the broaden light absorption of 2% Cu-WC/W materials, the optical measurements were investigated.

Figure 3a illustrates characteristic absorption spectra of in-situ synthesized catalytic samples. The absorption peak of WC/W primarily locates 420 to 550 nm, indicating it can accumulate light energy mainly in the visible range. This is in sharp contrast with previous results those showed very flat or negligible absorption spectra for metallic carbides [29, 55, 56]. However, the metallic Cu NPs shows very broad spectrum peaking at 500 nm and a weak shoulder at 850 nm, indicating the significant light absorption ability. Impressively, the weak shoulder at 850 is a distinct feature of Cu NPs, unfolds its near infrared responsive nature [57]. When WC/W NPs hybridized with different weight ratios of Cu NPs, it was revealed that 2% Cu-WC/W samples retain the characteristics peaking position as similar to Cu, covering full solar spectrum from 300 to 1100 nm [57]. This possibly associated with the wide Cu NPs size distribution profile before (Figure S8) and after (Figure S7) the WC/W NPs hybridization. Such strong light absorption capacity of 2% Cu-WC/W could be the indication of LSPR in the composite [57]. Note that the LSPR features of Cu NPs is strongly dependent on NPs sizes. It was highlighted that as NPs sizes gets smaller, the Cu NPs shows broad solar light absorption resulting in strong LSPR effects, whereas the resonance absorption efficiency gets weaker as NPs sizes increases because of the scattering effects [58, 59]. For example, with 10 nm size of Cu NPs, it was exhibited that the Cu NPs can accommodate broad solar light absorption from 300 to 900 nm

with absorption efficiency reaching to 99.4% while such light absorption efficiency was at 98.9% when Cu NPs size was 23 nm at the same wavelength range [58]. Another study found that with 15 nm of size, Cu NPs shows very wide solar absorption in the range 250-2250 nm [60]. In these examples, the materials were in the core-shell structure where Cu NPs act as core side and C as shell side. The presence of C as a shell in these investigations has two main goals: to protect the Cu NPs from being oxidized and facilitate the light absorption performance of the core-shell nanostructure [61, 62]. These results are direct indication that the in-situ formed Cu NPs with carbon coverage within this study is subjected to reveal the well-protected metallic phase of copper, thus enabling its broad solar light absorption. Therefore, the utilization of large fraction of the abundant solar flux ranging from UV-vis and near-infrared photons over 2% Cu-WC/W is feasible, which can boost the photocatalytic activity via plasmonic hot electron transfer to the catalytic reactive site.

Figure 3b, c shows complex refractive index and extinction co-efficient of Cu and WC samples, respectively, to provide further information on optical properties. The refractive index (n) is the measure of the reduction rate of the speed of light in the medium [63] whereas extinction co-efficient (k) is the measure of how fast light energy lost in the materials. Between 400 to 600 nm, the values of n is increasing whereas k achieved steady state following declining characteristics beyond 600 nm, reaching to almost zero value at near infrared (NIR) region, supporting strong light polarization phenomena due to LSPR [63, 64] for Cu sample (Figure 3b). The n and k values of WC sample (Figure 3c) against wavelength shows that WC could harvest visible frequencies starting above 400 nm to entire NIR region. Parallel observation was marked for metallic W which reveals poor solar light harvesting capacity (both n and k values of W is higher than bare Cu and WC samples) as shown in Figure S11. It is explicitly evident that bare Cu NPs sample, with lower n and k than WC and W, shows the improved light harvesting features as compared with WC and W samples.

Figure 3d, e shows real (ε_r) and imaginary (ε_i) part of the dielectric properties of Cu and WC samples. In principle, the value of ε_i can describe the molecular flow of photoexciated charge carrier (electron-hole) energy and dictate the LSPR dissipation pathway at NPs surface junction [65, 66]. As displayed, Cu has smaller ε_i value as compared with WC in the entire visible spectrum, indicating that the probability for the energetic charge carriers from Cu's LSPR to be adsorbed by the neighbouring WC. A significant difference in the context of dielectric properties of metallic W was noticed as compared with Cu and WC sample which disclose larger ε_r and ε_i values as wavelength enhances (Figure S12), supporting the fact that solar light harvesting behaviour is mainly associated with Cu and WC NPs. For a given multimetallic plasmonic nanohybrid system, there are two ways the photoexcited charge carriers could be formed and extracted from plasmonic NPs to surrounding materials: indirect and direct ways [66]. Under indirect way, the hot electron-hole pairs are generated within the plasmonic metal and those with enough energy transfer over to the attached materials, while the rest will be thermalized within the metal. In the direct way, the hot electron-hole pairs are directly generated near the interface regions between plasmonic metal and its attached materials [65, 66]. Such hot charge carriers will initiate the redox reactions with the nearest adsorbate molecules. However, to get the best of the catalytic performance, it is therefore necessitate to optimize the hot carrier generation and their distribution that highly depends on materials nano-geometry, optical properties, electronic structures, and the plasmon energy [67].

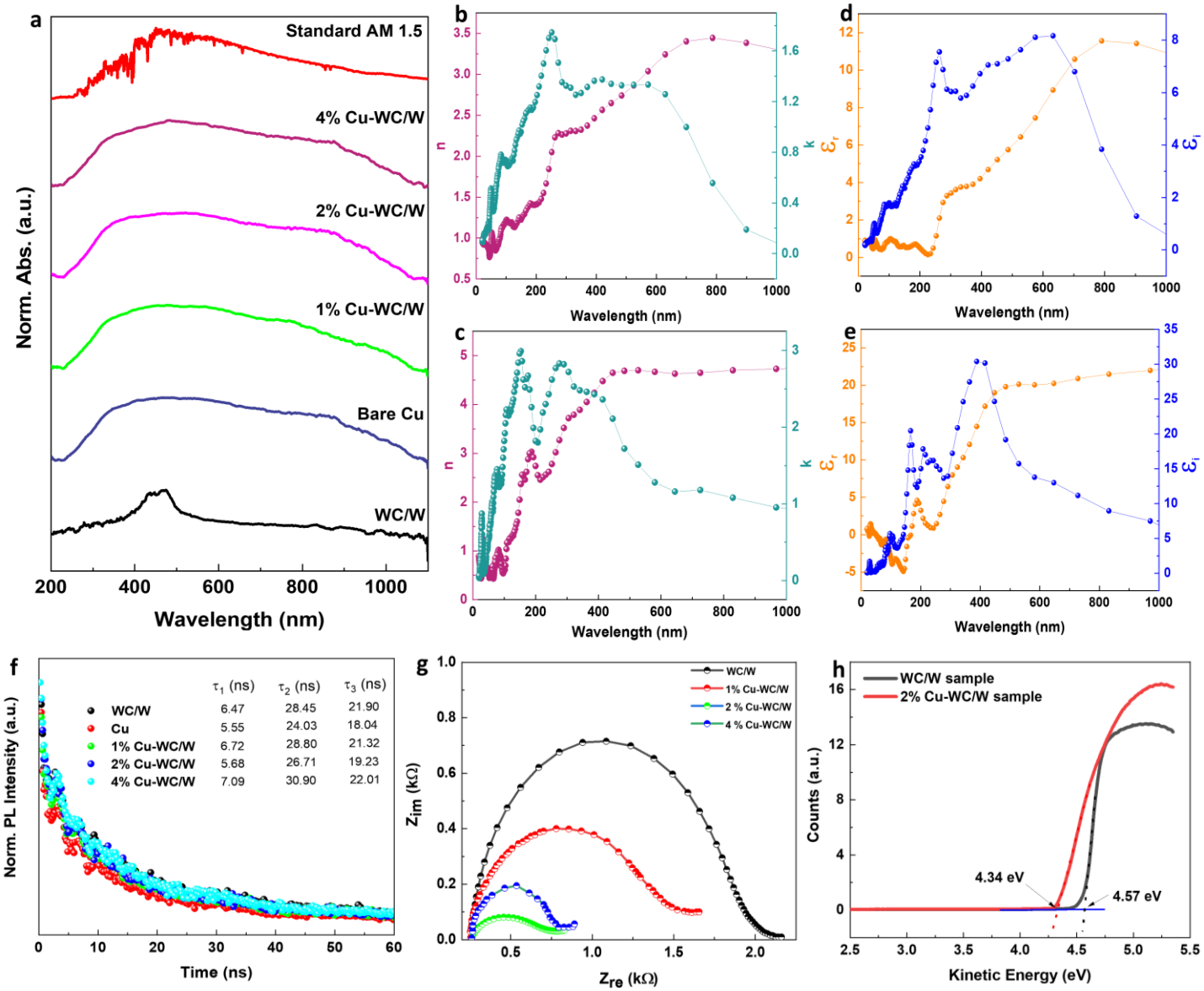

Fig. 3 | Optical and elecrical behaviours of the studied plasmonic photocatalysts. (a) Normalized absorption spectrum of WC/W, Cu, and Cu-WC/W photocatalysts, (b, c) Refractive index (n) and extinction co-efficient (k) versus wavelength for Cu and WC sample, respectively, (d, e) dielectric properties of Cu and WC sample, respectively, (f) TRPL profile of WC/W, Cu, and Cu-WC/W samples at 517 nm exitation and the inclusion of summarized average lifetime (τ_3) of the carriers (g) Nyquist plot of WC/W and Cu-WC/W, and (h) UPS profile for WC/W and 2% Cu-WC/W samples.

Theory suggests that under plasmonic excitation at resonant illumination condition, the photoinduced charge carriers dissipate their stored energy to the reactant molecules those are close proximity of the Fermi level of metal [67, 68]. Once these molecules are excited enough, their chemical bond activation and hence breaking are subsequently initiated on the surface of plasmonic NPs. These multi-facet activities is strongly reliant on the charge carrier's dynamics and their probabilistic participation to these photocatalytic activities. We examined the time-resolved photoluminescence (TRPL) of 2% Cu-WC/W NPs to disclose the plasmon-mediated charge carrier separation and recombination processes and far-reaching influence on photocatalytic CH_3OH dehydrogenation (Figure 3f). We used excitation wavelengths at 517 nm considering ???. The corresponding mathematical fitting of TRPL data was done by using bi-exponential equation (Note S2). As observed, the average carrier lifetime of the optimized 2% Cu-WC/W NPs was shorter (19.23 ns) than that of WC/W sample (21.90 ns) but much higher than pure Cu sample (18.04 ns) at 517 nm excitation. On the flipside, 1% Cu-WC/W (21.32 ns) and 4% (22.01 ns) Cu-WC/W samples have comparable charge carrier lifetime as WC/W sample. We assumed that the shortened charge carrier lifetime of 2% Cu-WC/W sample could be associated with effective spatial charge transfer and separation across the heterostructure nanointerface [69-71] whereas the high density reaction sites could afford the LSPR enhancement effects from broad light absorption feature of Cu NPs, which ultimately suppress the electrons and holes recombination process, leading to improved photoactivity [8, 72]. Another way, the local electric fields of LSPR regulates the generation of spatially inhomogeneous electron-hole pairs in close proximity of metallic Cu NPs. This means at the locale of Cu, the plasmonic excited charge carrier at given wavelength can access shorter diffusion path length to be available on WC active sites to generate H_2 energy from photocatalytic pure CH_3OH decomposition. By this way, we postulate that the plasmonic nanohybrids effectively increased the photooxidation activity of CH_3OH as long as the

probability of electron-hole pairs recombination remains slower than that of the probability of charge carriers to reach the reaction sites. However, the prolong lifetimes of the other studied samples resemblance the photoinduced charge carriers could not be rapidly transferred and thus, resulted in charge recombination. Parallel investigation was also reported similar charge carrier lifetime phenomenon that causes improved photoactivity at the nanointerface [73, 74]. An extremely deep and satisfying intuitive observation on charge carrier kinetics at the plasmonic nano-heterointerface was made by exploiting electrochemical impedance measurements as shown in Figure 3g. Evidently, the radius of the semicircle of WC/W sample is largest as compared with 1, 2, and 4% Cu-WC/W samples. More broadly, the characteristics semicircular spectra of 2% Cu-WC/W samples is compressed significantly, signalling improved charge carrier kinetics at plasmonic NPs interface. This rationalizes the idea that the integration of conventional plasmonic Cu metal with WC/W NPs may emanate very unconventional plasmonic nanohybrids which has potency to boost the photochemical reaction. The photoinduced charge carrier kinetics at the plasmonic nanohybrids interface have strong impact on plasmon driven chemical reaction which requires a fine-balancing of the work function (WF) of the catalysts. A delicate balancing of WF permits to achieve appropriate energy level alignment, establishing an energy equilibrium between Cu NPs and the metallic WC/W junction, resulting built-in charge carrier migration across the plasmonic nanohybrids interface. Ultraviolet photoelectron spectroscopy (UPS) measurement was performed to get insights on WF before and after Cu loadings on WC/W NPs as shown in Figure 3h. The extrapolation of corresponding UPS kinetics profile yielded WF values of 4.57 and 4.34 eV for WC/W and 2% Cu-WC/W samples, respectively, relative to vacuum. These results correspond to averaged WF of the composites. As the reported WF of metallic Cu is 4.1- 4.5 eV [75], lower than that of WC/W, it is reasonable the WF of 2% Cu-WC/W was reduced slightly after loading Cu onto WC/W

Sustained photocatalytic activity under plasmonic excitation at solar light irradiance conditions is the central objective of this work which has industrial significance. Before performing stability test, we have examined various working conditions and their impact on H_2 formation from pure methanol including Cu loadings (Figure S1), noble free metals addition (Figure S2), and illuminated light energy (Figure S3). A remarkable plasmon induced photocatalytic efficiency was distinguishable from 2% Cu-WC/W NPs over other studied catalysts under the same working conditions. As depicted in Figure 4a, we measured the H_2 volume for six consecutive cycles whereas each cycle sustained for about total 168 hours by employing AM 1.5 G filter. The H_2 production was escalated over the illuminated time up to 120 hours where it attains plateau reaching to the end of cyclising period. This could be explained by the fact that the in-situ formed H_2 in the volume-constant sealed reactor will rise the gaseous partial pressure, resulting in sluggish methanol activities [1, 2]. Quantitatively, however, within first 2 hours of irradiance of solar light, the produced H_2 was 8.70 µmole which extends to 22.41 µmole after 120 hours reaction. In terms of photocatalytic efficiency, this can be expressed from 2176.66 to 93.37 $\mu mole.g^{-1}.h^{-1}$ (Figure S13) over identical illuminated time. Impressively, all six cycles were maintained their undifferentiated recyclability ensuring ~ 96 % of the initially observed activity, equalizing more than 1000 hours of endurability (Figure S14), which has been rarely reported for this reaction up to date (Table S1). A comparison between WC/W and 2% Cu-WC/W sample highlights increased H_2 activity by almost 14 folds while such comparison exceeded over 47 magnitude between bare Cu and the optimized composite sample (Figure S2). Estimate of solar to hydrogen conversion efficiency was 2.37% indicating a sizeable volume of incident photon energy (11.20%) was utilized (Note S3, 4). This outstanding unsurpassable photocatalytic performance attributes to the highly stable nano-heterointerface between plasmonic Cu NPs and the WC/W NPs junction which altogether shows an uncommon promotional impact on the active sites on the catalysts surface. Notably,

the broad light absorption feature of the 2% Cu-WC/W NPs is considered to be an determining factor for catalysis improvement, which proliferated/excited charge carriers with different (low to high) kinetic energy for redox reactions [67]. Following this excellent stability of 2% Cu-WC/C NPs, we have performed chopped photocurrent measurement at various illuminated conditions as shown in Figure 4 b, c. Substantial differences in photocurrent activities were observed at different illumination conditions. For example, the photocurrent at AM 1.5 G was increased by 36.42, 69.41, and 77.32%, as compared at 420, 700, and 800 nm, respectively (Figure 4c). Notably, at AM 1.5 G simulated sunlight conditions, the photocurrent from 2% Cu-WC/C NPs was enhanced by 96.56% as compared with bare WC/W sample (Figure S15). These results directly prove that with higher light absorption ability of 2% Cu-WC/W NPs at AM 1.5 G conditions, the plasmon driven visible-light photoresponsivity was larger. We hypothesize that under plasmonic excitation at resonant illumination conditions, the energetic charge carrier follows a synchronized pathway such that the separation of energetic holes finds CH_3OH molecules at junction interface to be oxidized whereas the transfer of hot electrons promotes protons reduction to generate H_2 at the WC surface.

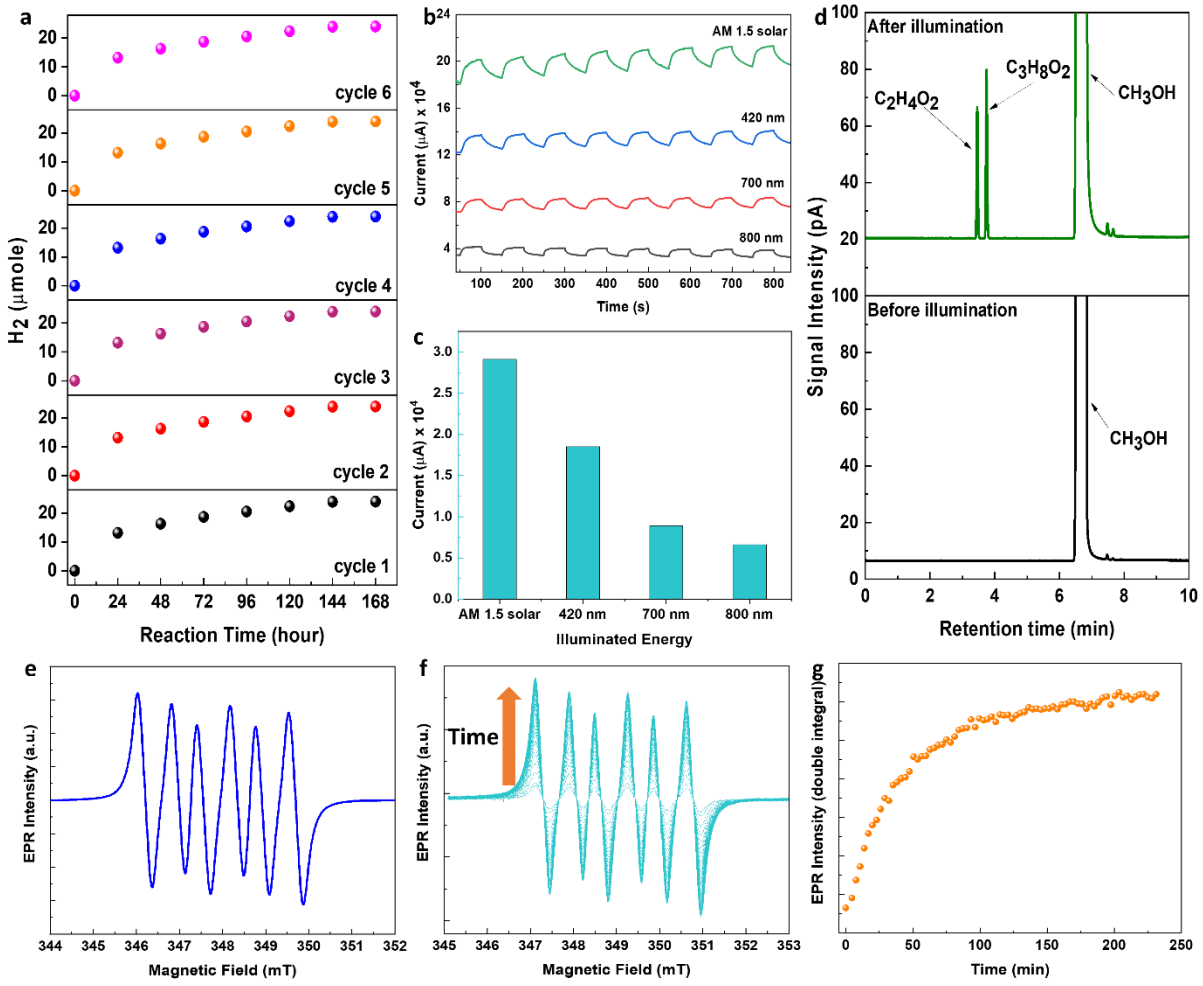

Fig. 4 |. Performance evaluation over plasmonic 2% Cu-WC/W catalysts. (a) H_2 evolution for six consequtive cycles, (b) Photocurrent at various wavelengths as a function of the time when light was on or off at 1.0 V against Ag/AgCl electrode in 0.1 M KOH aqueous solution cointaining pure CH_3OH. (c) Photocurrent at various illuminated wavelength, (d) Identified liquid products before and after illumination, (e) Electron paramagnetic resonance (EPR) profile for photodecomposition of methanol, (f) High resolution raw EPR spectra over 2% Cu-WC/W sample and the arrow mark represents time scale from starting point, and (g) kinetic profile of produced free radicals. Each of the data point in kinetic profile is representing each of the raw EPR spectra of figure (f).

Assisted by gas chromatography (GC) experimentation, we observed methylal ($C_3H_8O_2$) and methyl formate ($C_2H_4O_2$) as a liquid product alongside of self-separable H_2 gas. A cross-checking of this outcome was also verified by nuclear magnetic resonance spectroscopy (NMR) measurement (Note S5, Figure S16). Selectivity is a descriptor to explain the

preferential product formation in the system. So, selectivity of these products was estimated to be 80.94% for $C_3H_8O_2$ whereas it was 19.06% for $C_2H_4O_2$ (Note S6, Figure S17-20). As we did not observe any other carbon related products irrespective of their formation type (gaseous or liquid), we include the notion inclusively that the plasmon induce CH_3OH decomposition into H_2 is completely avoiding CO_x products formation (Note S7, Figure S21) even under such high efficiency, which affords benefits over conventional thermo-catalytic processes [2].

Methanol dehydrogenation into H_2 without forming any sort of environmental pollutants in presence of solar light proceeds selectively with complex steps which require the breakage of O-H bonds from CH_3OH [1, 2]. Other bonds breakage such as C-H is impracticable from thermodynamics standpoints. When CH_3OH breaks down into H_2 and HCHO via O-H route, the free radicals were reasonably formed within liquid methanol solution under solar illumination. Computing relevant hyperfine coupling (HFC) constants is a direct measure of validating the type of free radicals involved in the experiments. We noticed that the resolved HFC values a_N = 13.6 Gauss and a_H = 7.8 Gauss, revealing that the CH_3OH decomposition sourced CH_3O^* as a free radicals (Figure 4e) as confirmed by electron paramagnetic resonance (EPR) measurement which is in parallel to previous results [1, 2]. No activity in producing the free radicals of WC/W sample or radical trapper (5,5-dimethyl-1-pyrroline N-oxide, DMPO) was marked (Note S8, Figure S22) under identical conditions, confirming the assertion that the hybridization between plasmonic Cu NPs and WC/W NPs is crucial which likely to responsible to drive H_2 and other products formation preferentially. To gain more insights on radical behaviour upon light illumination, we performed time dependent in-situ EPR test as shown in Figure 4f, g. Starting in dark conditions (first EPR spectra in Figure 4f when t = 0), the radical was absent, i.e., the accumulation of DMPO-OCH_3* adduct upon switching off the light source was barely observable or at subdetection limit. As time progressed, the magnitude of the spectra was more intense corresponding appreciable free radical accumulation over 2% Cu-WC/W

NPs sample under light irradiance. Accumulation of DMPO-OCH_3* adduct was much stronger at least for 120 minutes (Figure 4g) while such radicals formation was gradually continued for rest of the experiment. This illustrative evidenced confirms that the in-situ prepared plasmonic 2% Cu-WC/W NPs was exhibited excellent feedback towards oxy-centred radical formation from pure CH_3OH under light illumination, which is critically important in understanding the reaction mechanism of CH_3OH dehydrogenation. Note that the kinetic curves shown in Figure 4g is a complex measure of H_2 production from plasmonic CH_3OH dissociation activities and it is not solely representative time profile of the tested reaction. Instead, the displayed kinetic results from a complex interaction of the rate of formation of CH_3O*, the rate of trapping of CH_3O* by DMPO, and the rate of decay of the DMPO-OCH_3* adduct.

Overall, we infer from above catalytic characterization, optical properties, performance and long-standing durability experimentation that the in-situ synthesized plasmonic 2% Cu-WC/W NPs would induce chemical interactions of the CH_3OH molecules to produce cleaner H_2 energy without forming any CO_x products is interlinked with its coupling effects of strain and electric fields perturbed activities at the nano-heterointerface. Plasmon driven such interface activities will be further substantiated and prediction on how catalytic structure of 2% Cu-WC/W NPs impact on the reaction mechanism will be made next.

4. Reaction Mechanism Study

Plasmonic excitation upon visible light illumination can result in energetic charge carriers (hot e^--h^+ pairs) generation on the NPs surface which has been studied previously in the perspective of chemical reactions transformations [65, 76, 77]. The extraction of charge carriers and their directional flow towards the catalytic sites in reactive environment could be multistep under plasmonic excitation when considering multimetallic nanohybrid system, for example, Cu-WC/W NPs in this work. We postulated that methanol underwent multi-hole assisted oxidation

processes to yield H_2 under plasmonic excitation at the NPs junction via direct and indirect charge transfer mechanism [66, 77] at solar light illumination conditions as expressed in reaction 1 and 2. We hypothesized that hot hole mediated CH_3OH oxidation over plasmonic Cu-WC/W NPs can be influenced by multiple factors: (1) modulation of reaction pathways of WC catalyst under perturbation by by strain field from W template and electric field from WC LSPR itself, (2) broadband absorption from plasmonic Cu NPs generates energetic charge carriers (hot e^--h^+ pairs) in Cu which flow to the neighbouring WC catalyst because of WC's higher imaginary part of dielectric function than Cu NPs [66, 77], and (3) Cu's LSPR results in direct energetic charge carrier formation at Cu-WC interface via plasmon decay. A cooperative and mutual efforts of these factors play role in methanol oxidation with proton reduction to H_2 fuel at Cu-WC interfaces.

$$CH_3OH^* + h^+ \rightarrow CH_3O^* + H^+ \quad (1)$$

$$CH_3O^* + h^+ \rightarrow HCHO^* + H^+ \quad (2)$$

$$H^+ + H^+ + 2e^- \rightarrow H_2 \quad (3)$$

Once the reaction steps (1) completed by consuming one hole on WC NP surface, the intermediate, CH_3O^* (methoxy species) experiences further oxidation steps (2) to yield formaldehyde that evolved in existence of second hole. The photoexcitation cycle completed by capture of $2e^-$ to reduce the two available protons for H_2 fuel in (3). In these processes, the formation of second e^--h^+ pair (which provide the second hole for step 2) is critical which needs to be formed within few-μs timescale (the lifetime of CH_3O^* is around 4 μs in CH_3OH solution [78]) on NPs immediately after the one hole driven CH_3OH oxidation process. Nevertheless, the availability of HCHO in excess of methanol in the solution to yield methylal ($CH_3OCH_2OCH_3$) via combination process [79] while the successive decomposition of CH_3O^* forms other intermediates species those participate into multistep reaction pathways to generate methyl formate, $HCOOCH_3$ (Note S9) [80] is likely to proceed.

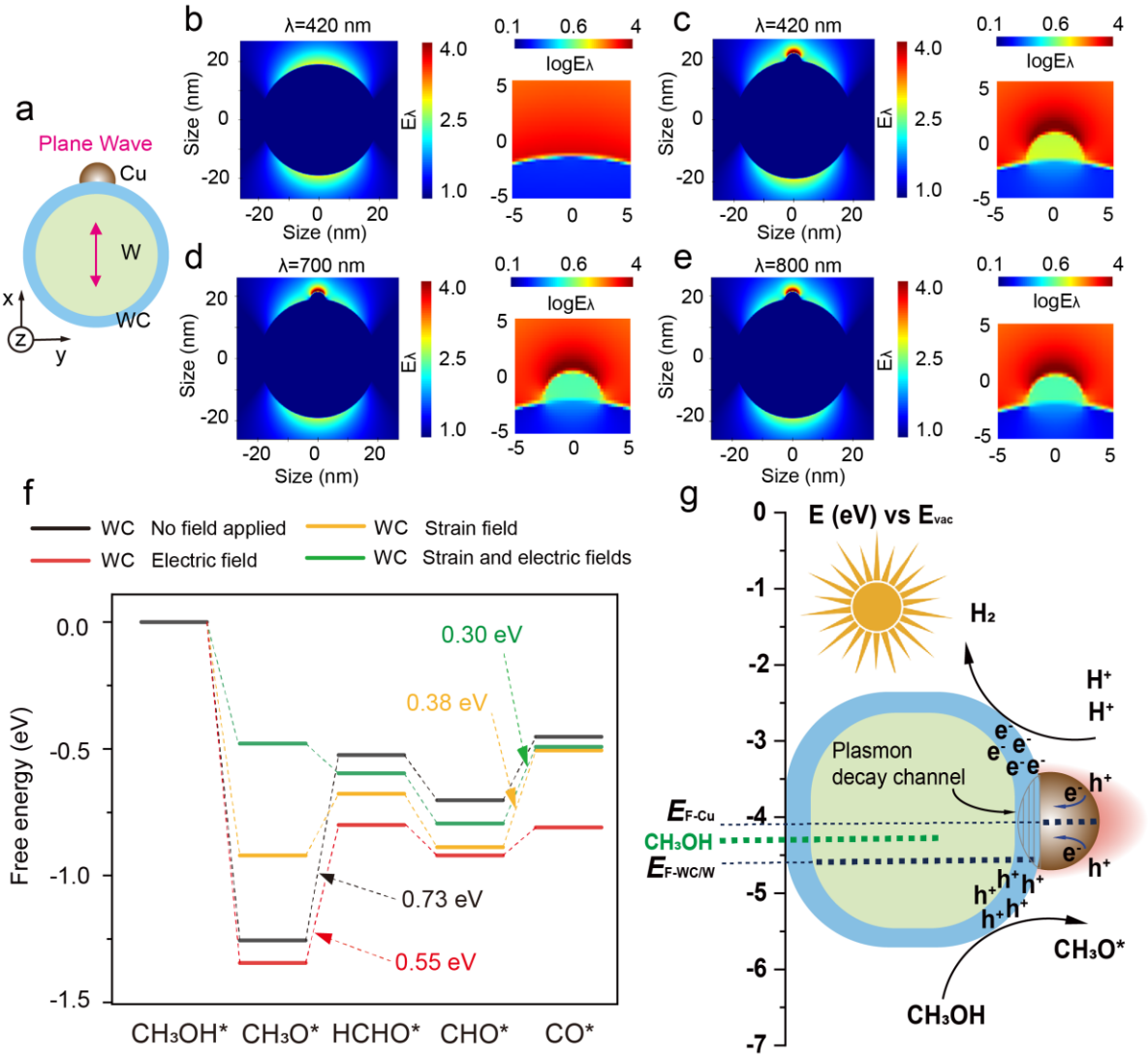

Fig. 5 | (a) Schematic representation of the Cu NP embedded on a WC/W substrate used in finite-difference time-domain (FDTD) simulation. (b)-(e) Schematics (left) and partial zoom (right) showing the enhancement of electric field intensity induced by WC/W and (c)-(e) wavelength effects on the distributions of the electric field strength for the Cu NP embedded on a WC/W substrate. The enhancement of electric field intensity induced by introducing Cu NPs is compared by (b) and (c). (f) Free energy diagram for methanol dehydrogenation calculated by DFT, where the perturbations from the strain field (??%), electric field (???V/m under ×2 enhancement) or both were applied. (g). Photocatalytic mechanism insights of dual-fields tuned WC activity in Cu-WC/W junctions for selective methanol to H_2 and multi-carbon products. The elevated local electric field surrounding the Cu NP surface are schematically presented. The Fermi levels of WC/W and Cu, and the oxidation energy level (~ 4.3 eV) of

methanol molecule relative to the vacuum energy level are indicated. Plasmon decay channels show WC layer's absorption/dissipation of energetic charge carriers from plasmonic Cu layer.

We performed computational investigation via finite-difference time-domain (FDTD) simulation and density functional theory (DFT) to study LSPR's local electric field distribution and unveil the effects of microenvironments (stain field and/or electric field) on the underlying CH_3OH dehydrogenation reactions at the Cu-WC/W NPs. In the present work, as the photoreaction is processed by the same solar light illumination over homogeneously dispersed Cu-WC/W NPs in methanol solution, the irradiance conditions onto the catalysts from different directions remains identical. To discover plasmonic behavior from FDTD, our simulation considered different wavelength and direction of the incident light relative to the Cu NPs mounted on WC/W, as shown in Fig. 5a-e and Figure S23. As widely generalized that upon light illumination, the incident photons interact with the conduction electrons of the plasmonic metal NPs resulting in the excitation of LSPR. The LSPR acts to confine the photon energy and generate strong local electric fields via enhanced light absorption at the surfaces of metallic NPs [77, 81]. The energy of these elevated fields can be dissipated through either radiative re-emission of photons, or nonradiative excitation of energetic charge carriers (hot e^-/h^+) which could transfer to nearby materials. On the other hand, these elevated fields could perturb/tailor the surrounding reaction microenvironments of attached catalysts. When it comes to our multimetallic Cu-WC/W plasmonic nano system, Cu NPs exhibit the obvious LSPR after mounted onto WC/W. The local electric field intensity was enhanced and doubled as shown in Figure 5b-e. Especially, the tops near the Cu NPs are covered by the extended electric field of the Cu LSPR, as shown in Fig. 5c-e, indicating that the Cu NPs introduce more the light absorption and provide more carriers for the CH_3OH dehydrogenation on WC. Note that theoretical analysis suggests that the Cu NPs could produce strong electric field from LSPR but underperformed in CH_3OH dehydrogenation due to its relative high reaction energy barrier

(0.73 eV in Figure S24). Likewise, the relative high reaction energy barriers of 0.73 eV and 0.41 eV were also recorded over freestanding WC and W NPs, respectively (Fig 5f, Figure S25).

Quest to understand the strain effects on CH_3OH dehydrogenation reactions, we performed DFT to compute the free energy of reaction pathways. The compressive strain on WC from W due to lattice mismatch has appreciable impact on the reduction of reaction energy height (Figure 5f). Without any external field perturbation (black pathways), the first dehydrogenation step ($CH_3OH^* \rightarrow CH_3O^*$) is easily occurred on WC which is an exothermic in nature. Next, the dehydrogenation of CH_3O^* face the energy barrier of 0.73 eV, which is the rate-determining step ($CH_3O^* \rightarrow HCHO^*$) due to the hindrance of dehydrogenation of C saturated bonds for the reference WC under no external field perturbation. However, when strain field applied on WC, the rate-determining step shift to $CHO^* \rightarrow CO^*$ (orange pathways) from $CH_3O^* \rightarrow HCHO^*$. The photocatalytic rate-determining step shift caused by different lattice spacing's has been reported elsewhere [82, 83]. With lattice misfits, the WC NPs shows reaction barrier at 0.38 eV, which is much lower than the barrier 0.73 eV relative to WC (black pathways), indicating the importance of strained mediated CH_3OH dehydrogenation process. We studied the electric field effect from WC LSPR itself based on the enhanced electric field intensity simulated by FDTD to verify the second factors abovementioned. The complete free energy diagram was calculated by DFT to confirm the influence of the electric field (Figure 5f, red pathways). As noticed, WC under electric field conditions, the rate-determining step ($CH_3O^* \rightarrow HCHO^*$) has the energy barrier of 0.55 eV which is lower than 0.73 eV relative to WC. Impressively, when electric field and strain field are combined, the effect on WC catalysis is greatly enhanced with the reaction barrier reduced significantly (green pathways, Figure S26). The reaction steps prior to the $CHO^* \rightarrow CO^*$ step are all exothermic processes, favoring the methanol oxidation with releasing the protons for H_2 production, whilst the reaction height

get reduced to 0.30 eV for CHO* → CO* step. This energy barrier is phenomenal to prohibit the further oxidation of CO* species to form any CO and/or CO_2 in the reaction resulting the zero-carbon emission which is perfectly consistent with experimental observation (Figure S21). However, the formed CO* species could combined with the available intermediates to form methyl formate ($HCOOCH_3$) which has been followed-up later. Note here, the Cu LSPR induced extra two-time enhancement of local field, i.e. four time enhanced compared with the incident light, at WC surface. Such ×4 enhanced electric field was also combined with strain field in studying their coupled effect on the reaction pathways (Figure S26-b). The results indicated the effect from ×4 electric field does not change much from that under ×2 electric field. Mechanistic study reveals that the kinetics of methanol decomposition on Cu-WC/W NPs hybrid system is mainly attributed to the combined perturbation of the strain and electric strain fields in WC and energetic charge carriers supply from Cu LSPR after broadband solar absorption, which makes the oxidation of CH_3O* into HCHO* easier, while the adsorption of CH_3O* on the WC surface through a single field is not enough to significantly reduce the reaction energy barrier. On the other hand, the strain field induced rate-determining step change from CH_3O* → HCHO* to CHO* → CO* afore-discussed would help to prolong the dehydrogenation and release more H^+ to form H_2, greatly improving the production of H_2 while suppressing the CO and/or CO_2 formation simultaneously. The DFT calculation unveils that the efficient CH_3OH dehydrogenation to zero-emission H_2 fuel is attributed to synergistic microenvironments tuning by the dual (strain and electric) fields and rich charge carrier supply from Cu-WC/W NPs hybrid system, which has been schematically represented in Figure 5g. The Fermi level, i.e. work function, of - 4.57 eV from WC/W, as indicated by black dot line, is more negative to that (~ -4.3 eV) of the methanol oxidation potential, indicated by green dot line. This favours the energetic charge carriers/holes to oxidize methanol molecules near the surface of WC. Based on our observed great performance enhancement after loading Cu, we

deduce the energetic charge carriers (hot e^--h+ pairs) will flow and dissipate the energy from Cu to WC via plasmon decay channel because the higher imaginary part of dielectric function of WC than Cu NPs aforementioned (Figure 5g). In addition, as WC and Cu NPs are in close proximity, the higher energy absorption of WC shell from localized field intensities of Cu LSPR at the junction could push up more e^-- h+ formation [65] via plasmon decay there. Broadly, the NPs with magnified field magnitude at LSPR wavelengths are highly effective in dissipating energy via localized absorption process since a larger value of ε_i relative to the plasmonic metal can regulate the energy flow as their geometric configuration can drive the energy to the chosen location [77].

Further to the above factors, methanol itself does play vital roles in the oxidation process to form H_2 with varied chemical products. Methanol is recognized as a good hole scavenger which could induce multi-hole reaction steps due to hot hole localization [76] on the surface of WC NPs. In other words, methanol has strong electron-donating capacity on the NPs surface. This corollary indicates that the photoexcited charge carriers under solar light illumination could transfer the excitation to the CH_3OH molecules, with energetic holes and electrons to drive the methanol oxidation and the subsequent proton reduction to H_2 fuel. Parallel observations were made previously in which the presence of hole scavenger could promote the transient photoexciation at the NPs-molecule interface [84, 85]. Moreover, the concentration of hole scavenger can affect the multi-hole driven process, as highlighted that the higher the hole scavenger concentration, the higher the rate of multi-hole oxidation as well as larger the multi-electron reduction process [86]. Note that the Cu-WC/W photocatalysts in this work were suspended in the excess pure methanol (purity ~ ≥ 99.9%) during methanol dehydrogenation. Collectively, all these factors play role in triggering the CH_3OH oxidation at the interface as the highly energetic holes interact with the adsorbed CH_3OH molecules, yielding H_2 along with industrially relevant products.

5. Conclusion

We demonstrated the first synthesis of non-traditional plasmonic nanohybrid structure between Cu and WC/W NPs using high temperature process. We optimized the different working parameters and found the applicability of 2% Cu-WC/W NPs in liquid CH_3OH dehydrogenation at room temperature among the in-situ prepared catalytic materials. We made the assertion that the semi-coherent heteroepitaxial growth of WC on W under the carburization process would introduce disruptive features when hybridize with plasmonic Cu NPs. Cu nanoplasmon possesses broad solar spectrum which have strong electric field responsiveness under excitation that results in the formation of distinct charge carrier pairs and delocalization towards reacting methanol molecules at the catalysts interface. As a result, the photocatalytic H_2 production efficiency was found high over 2% Cu-WC/W NPs (2176.66 $\mu mole.g^{-1}.h^{-1}$) as compared with bare WC/W NPs (156.83 $\mu mole.g^{-1}.h^{-1}$) under solar light irradiance and long-standing photocatalytic activities were achieved that surpass more than 41 days operational reaction conditions from six subsequent tests. Further we highlighted that the longevity of the photoreaction would be recoverable by almost ~96 % and such highly stable reactions is free from CO_x formation. We showed that liquid methanol is not only produced self-separable H_2 gase but also two other energy intensive products those have industrial relevance. Experimentally, we found that the presence of strain effect in WC shell due to W could facilitate the CH_3OH oxidation by energetic hole when plasmonic Cu NPs interact. Computational studies show that the kinetics of methanol decomposition on Cu-WC/W NPs hybrid system is mainly attributed to the combined perturbation of the electric and strain fields, which makes the oxidation of methanol is much easier with significantly reduced energy

barrier. We believe that the underlying reaction mechanisms highlighted within this study will foster the engineering of other multicomponent plasmonic nanohybrid structure that would have manifold advantages than conventional materials. This work will be a guiding principle in plasmon-mediated sustainable solar fuel production because the prepared materials is sourced from abundant and inexpensive Cu and WC metal.

Author Contributions

N. Uddin did the synthesis, all experiments, analysed the experimental data, and wrote the manuscript. Julien Langley and Dr. Nick Cox performed the EPR experiments, analyzed those experimental data and co-wrote the manuscript. Dr. Hieu T. Nguyen performed the PL experiments. Dr. Zongyou Yin designed the whole idea for this work, outlined the expected experiments, analysed the experimental data, and co-wrote the paper. All of the authors discussed the results and reviewed the manuscript.

Declaration of Competing Interest

The authors declare that they have no known competing financial interests or personal relationships that could have appeared to influence the work reported in this paper.

Acknowledgement

The authors gratefully acknowledge the support from the ANU Futures Scheme (Q4601024),. MLC acknowledges an ARC Laureate Fellowship (FL170100041).

Appendix A. Supplementary data

Supplementary material related to this article can be found, in the online version.

Reference

1. Pang, Y., et al., *Colloidal Single‐Layer Photocatalysts for Methanol‐Storable Solar H2 Fuel.* Advanced Materials, 2019. **31**(49): p. 1905540.
2. Uddin, N., et al., *Zero-emission multivalorization of light alcohols with self-separable pure H2 fuel.* Applied Catalysis B: Environmental, 2021. **292**: p. 120212.
3. Mitchell, S., et al., *Nanoscale engineering of catalytic materials for sustainable technologies.* Nature Nanotechnology, 2021. **16**(2): p. 129-139.
4. Leclercq, L., et al., *Catalytic properties of transition metal carbides: II. Activity of bulk mixed carbides of molybdenum and tungsten in hydrocarbon conversion.* Journal of Catalysis, 1989. **117**(2): p. 384-395.
5. Pang, M., et al., *Activated carbon supported molybdenum carbides as cheap and highly efficient catalyst in the selective hydrogenation of naphthalene to tetralin.* Green Chemistry, 2012. **14**(5): p. 1272-1276.
6. Claridge, J.B., et al., *New catalysts for the conversion of methane to synthesis gas: molybdenum and tungsten carbide.* Journal of catalysis, 1998. **180**(1): p. 85-100.
7. Zheng, W., et al., *Experimental and theoretical investigation of molybdenum carbide and nitride as catalysts for ammonia decomposition.* Journal of the American Chemical Society, 2013. **135**(9): p. 3458-3464.
8. Huang, W., et al., *Metallic tungsten carbide nanoparticles as a near-infrared-driven photocatalyst.* Journal of Materials Chemistry A, 2019. **7**(31): p. 18538-18546.
9. Liu, Z., et al., *Photoactivity and Stability Co‐Enhancement: When Localized Plasmons Meet Oxygen Vacancies in MgO.* Small, 2018. **14**(48): p. 1803233.
10. Biggins, J.S., S. Yazdi, and E. Ringe, *Magnesium nanoparticle plasmonics.* Nano letters, 2018. **18**(6): p. 3752-3758.
11. Marbella, L.E., et al., *Correlating Carrier Density and Emergent Plasmonic Features in Cu2–x Se Nanoparticles.* Nano letters, 2017. **17**(4): p. 2414-2419.
12. Quiroz, J., et al., *Controlling reaction selectivity over hybrid plasmonic nanocatalysts.* Nano letters, 2018. **18**(11): p. 7289-7297.
13. Zhou, L., et al., *Aluminum nanocrystals as a plasmonic photocatalyst for hydrogen dissociation.* Nano letters, 2016. **16**(2): p. 1478-1484.
14. Marimuthu, A., J. Zhang, and S. Linic, *Tuning selectivity in propylene epoxidation by plasmon mediated photo-switching of Cu oxidation state.* Science, 2013. **339**(6127): p. 1590-1593.
15. Wang, Y., et al., *Ultrastable Plasmonic Cu-Based Core–Shell Nanoparticles.* Chemistry of Materials, 2020. **33**(2): p. 695-705.
16. Sang, L., S. Zhang, and Y. Gao, *Investigation of plasmonic Cu with controlled diameter over TiO2 photoelectrode for solar-to-hydrogen conversion.* International Journal of Hydrogen Energy, 2019. **44**(47): p. 25486-25494.
17. Aslam, U., S. Chavez, and S. Linic, *Controlling energy flow in multimetallic nanostructures for plasmonic catalysis.* Nature nanotechnology, 2017. **12**(10): p. 1000-1005.
18. Chen, S., et al., *Carbon-coated Cu-TiO2 nanocomposite with enhanced photostability and photocatalytic activity.* Applied Surface Science, 2019. **466**: p. 254-261.
19. Kimmel, Y.C., et al., *Effect of surface carbon on the hydrogen evolution reactivity of tungsten carbide (WC) and Pt-modified WC electrocatalysts.* International journal of hydrogen energy, 2012. **37**(4): p. 3019-3024.
20. Hara, Y., N. Minami, and H. Itagaki, *Synthesis and characterization of high-surface area tungsten carbides and application to electrocatalytic hydrogen oxidation.* Applied Catalysis A: General, 2007. **323**: p. 86-93.
21. Zhang, Q., et al., *A robust electrocatalytic activity toward the hydrogen evolution reaction from W/W 2 C heterostructured nanoparticles coated with a N, P dual-doped carbon layer.* Chemical Communications, 2019. **55**(65): p. 9665-9668.
22. Preuster, P., C. Papp, and P. Wasserscheid, *Liquid Organic Hydrogen Carriers (LOHCs): Toward a Hydrogen-free Hydrogen Economy.* Accounts of Chemical Research, 2017. **50**(1): p. 74-85.

23. Markiewicz, M., et al., *Environmental and health impact assessment of Liquid Organic Hydrogen Carrier (LOHC) systems–challenges and preliminary results.* Energy & Environmental Science, 2015. **8**(3): p. 1035-1045.
24. Tan, H., et al., *Enhanced photocatalytic hydrogen production from aqueous-phase methanol reforming over cyano-carboxylic bifunctionally-modified carbon nitride.* Chemical Communications, 2019. **55**(83): p. 12503-12506.
25. Lin, L., et al., *Low-temperature hydrogen production from water and methanol using Pt/α-MoC catalysts.* Nature, 2017. **544**(7648): p. 80-83.
26. Nomikos, G.N., et al., *Kinetic and mechanistic study of the photocatalytic reforming of methanol over Pt/TiO2 catalyst.* Applied Catalysis B: Environmental, 2014. **146**: p. 249-257.
27. Ravel, B. and M. Newville, *ATHENA, ARTEMIS, HEPHAESTUS: data analysis for X-ray absorption spectroscopy using IFEFFIT.* Journal of synchrotron radiation, 2005. **12**(4): p. 537-541.
28. Bennett, L., et al., *Electronic structure and catalytic behavior of tungsten carbide.* Science, 1974. **184**(4136): p. 563-565.
29. Jang, J.S., et al., *Role of platinum-like tungsten carbide as cocatalyst of CdS photocatalyst for hydrogen production under visible light irradiation.* Applied Catalysis A: General, 2008. **346**(1-2): p. 149-154.
30. Liang, S., et al., *Fabrication of CuW pseudo alloy by W–CuO nanopowders.* Journal of alloys and compounds, 2012. **516**: p. 161-166.
31. Li, Y., et al., *WC strengthened W–Cu nanocomposite powder synthesized by in-situ reactions.* International Journal of Refractory Metals and Hard Materials, 2019. **79**: p. 154-157.
32. Gong, Q., et al., *Ultrasmall and phase-pure W 2 C nanoparticles for efficient electrocatalytic and photoelectrochemical hydrogen evolution.* Nature communications, 2016. **7**(1): p. 1-8.
33. Zhang, C., et al., *Synthesis and thermal conductivity improvement of W-Cu composites modified with WC interfacial layer.* Materials & Design, 2017. **127**: p. 233-242.
34. Dong, L., et al., *Microstructure and properties characterization of tungsten–copper composite materials doped with graphene.* Journal of Alloys and Compounds, 2017. **695**: p. 1637-1646.
35. Katoh, M. and H. Kawarada, *Heteroepitaxial growth of tungsten carbide films on W (110) by plasma-enhanced chemical vapor deposition.* Japanese journal of applied physics, 1995. **34**(7R): p. 3628.
36. Zhang, J., et al., *Nonepitaxial growth of hybrid core-shell nanostructures with large lattice mismatches.* Science, 2010. **327**(5973): p. 1634-1638.
37. Habas, S.E., et al., *Shaping binary metal nanocrystals through epitaxial seeded growth.* Nature materials, 2007. **6**(9): p. 692-697.
38. Warren, A., A. Nylund, and I. Olefjord, *Oxidation of tungsten and tungsten carbide in dry and humid atmospheres.* International Journal of Refractory Metals and Hard Materials, 1996. **14**(5-6): p. 345-353.
39. Chan, G.H., et al., *Plasmonic properties of copper nanoparticles fabricated by nanosphere lithography.* Nano letters, 2007. **7**(7): p. 1947-1952.
40. Chen, Z., et al., *Eutectoid-structured WC/W2C heterostructures: A new platform for long-term alkaline hydrogen evolution reaction at low overpotentials.* Nano Energy, 2020. **68**: p. 104335.
41. Kim, I., S.-W. Park, and D.-W. Kim, *Carbon-encapsulated multi-phase nanocomposite of W 2 C@ WC 1− x as a highly active and stable electrocatalyst for hydrogen generation.* Nanoscale, 2018. **10**(45): p. 21123-21131.
42. Shao, M., et al., *WXy/g-C3N4 (WXy=W2C, WS2, or W2N) Composites for Highly Efficient Photocatalytic Water Splitting.* ChemSusChem, 2019. **12**(14): p. 3355-3362.
43. Xu, X., et al., *Enriching Hot Electrons via NIR-Photon-Excited Plasmon in WS2@Cu Hybrids for Full-Spectrum Solar Hydrogen Evolution.* Advanced Functional Materials, 2018. **28**(43): p. 1804055.

44. Huang, H.-B., et al., *Localized surface plasmon resonance enhanced visible-light-driven CO2 photoreduction in Cu nanoparticle loaded ZnInS solid solutions.* Nanoscale, 2020. **12**(28): p. 15169-15174.
45. Sang, L., et al., *TiO2 nanotube arrays decorated with plasmonic Cu, CuO nanoparticles, and eosin Y dye as efficient photoanode for water splitting.* Materials Chemistry and Physics, 2019. **231**: p. 27-32.
46. Kirsch, P. and J. Ekerdt, *Chemical and thermal reduction of thin films of copper (II) oxide and copper (I) oxide.* Journal of Applied Physics, 2001. **90**(8): p. 4256-4264.
47. Borfecchia, E., et al., *Evolution of active sites during selective oxidation of methane to methanol over Cu-CHA and Cu-MOR zeolites as monitored by operando XAS.* Catalysis Today, 2019. **333**: p. 17-27.
48. Paolucci, C., et al., *Dynamic multinuclear sites formed by mobilized copper ions in NOx selective catalytic reduction.* Science, 2017. **357**(6354): p. 898-903.
49. Korshin, G.V., A.I. Frenkel, and E.A. Stern, *EXAFS Study of the Inner Shell Structure in Copper(II) Complexes with Humic Substances.* Environmental Science & Technology, 1998. **32**(18): p. 2699-2705.
50. Du, X.L., et al., *Research progress on the indirect hydrogenation of carbon dioxide to methanol.* ChemSusChem, 2016. **9**(4): p. 322-332.
51. Yang, S.-C., et al., *Synergy between Ceria Oxygen Vacancies and Cu Nanoparticles Facilitates the Catalytic Conversion of CO2 to CO under Mild Conditions.* ACS Catalysis, 2018. **8**(12): p. 12056-12066.
52. Deng, S., et al., *Plasmonic Photoelectrocatalysis in Copper–Platinum Core–Shell Nanoparticle Lattices.* Nano letters, 2021. **21**(3): p. 1523-1529.
53. Ha, M., et al., *Multicomponent plasmonic nanoparticles: from heterostructured nanoparticles to colloidal composite nanostructures.* Chemical reviews, 2019. **119**(24): p. 12208-12278.
54. Tian, Y. and J. Toudert, *Nanobismuth: fabrication, optical, and plasmonic properties—emerging applications.* Journal of Nanotechnology, 2018. **2018**.
55. Ma, B., et al., *A novel earth‐abundant W‐WC heterojunction as efficient co‐catalyst for enhanced photocatalytic H2 evolution.* ChemCatChem, 2020. **12**(4): p. 1148-1155.
56. Ren, C., et al., *ZnSe nanoparticles with bulk WC as cocatalyst: A novel and noble-metal-free heterojunction photocatalyst for enhancing photocatalytic hydrogen evolution under visible light irradiation.* Applied Materials Today, 2020. **20**: p. 100731.
57. Zhang, P., et al., *In-situ synthesis of Cu nanoparticles hybridized with carbon quantum dots as a broad spectrum photocatalyst for improvement of photocatalytic H2 evolution.* Applied Catalysis B: Environmental, 2017. **206**: p. 328-335.
58. Xu, Y., et al., *Cu@C core-shell nanoparticles with efficient optical absorption: DDA-based simulation and experimental validation.* Results in Physics, 2020. **16**: p. 102885.
59. Chen, X., et al., *Systematically investigating solar absorption performance of plasmonic nanoparticles.* Energy, 2021. **216**: p. 119254.
60. Ren, L., et al., *Designing Carbonized Loofah Sponge Architectures with Plasmonic Cu Nanoparticles Encapsulated in Graphitic Layers for Highly Efficient Solar Vapor Generation.* Nano Letters, 2021. **21**(4): p. 1709-1715.
61. Li, H., et al., *Thermal synthesis of Cu@carbon spherical core–shell structures from carbonaceous matrices containing embedded copper particles.* Carbon, 2010. **48**(2): p. 464-469.
62. Lim, D.-K., et al., *Enhanced Photothermal Effect of Plasmonic Nanoparticles Coated with Reduced Graphene Oxide.* Nano Letters, 2013. **13**(9): p. 4075-4079.
63. Aziz, S.B., et al., *In situ synthesis of CuS nanoparticle with a distinguishable SPR peak in NIR region.* Journal of Materials Science: Materials in Electronics, 2016. **27**(5): p. 4163-4171.

64. Sakr, G.B., et al., *Optical spectroscopy, optical conductivity, dielectric properties and new methods for determining the gap states of CuSe thin films.* Journal of Alloys and Compounds, 2010. **507**(2): p. 557-562.
65. Linic, S., S. Chavez, and R. Elias, *Flow and extraction of energy and charge carriers in hybrid plasmonic nanostructures.* Nature Materials, 2021: p. 1-9.
66. Chavez, S., V.G. Rao, and S. Linic, *Unearthing the factors governing site specific rates of electronic excitations in multicomponent plasmonic systems and catalysts.* Faraday discussions, 2019. **214**: p. 441-453.
67. Brongersma, M.L., N.J. Halas, and P. Nordlander, *Plasmon-induced hot carrier science and technology.* Nature nanotechnology, 2015. **10**(1): p. 25-34.
68. Aslam, U., et al., *Catalytic conversion of solar to chemical energy on plasmonic metal nanostructures.* Nature Catalysis, 2018. **1**(9): p. 656-665.
69. Li, J., et al., *The Spatially Oriented Charge Flow and Photocatalysis Mechanism on Internal van der Waals Heterostructures Enhanced g-C3N4.* ACS Catalysis, 2018. **8**(9): p. 8376-8385.
70. Foo, W.J., C. Zhang, and G.W. Ho, *Non-noble metal Cu-loaded TiO 2 for enhanced photocatalytic H 2 production.* Nanoscale, 2013. **5**(2): p. 759-764.
71. Li, H., et al., *Cu nanoparticles hybridized with ZnO thin film for enhanced photoelectrochemical oxygen evolution.* Journal of Alloys and Compounds, 2018. **768**: p. 830-837.
72. Wang, S.L., et al., *2D WC/WO3 heterogeneous hybrid for photocatalytic decomposition of organic compounds with Vis–NIR light.* Advanced Functional Materials, 2018. **28**(11): p. 1705357.
73. Tong, R., et al., *Ultrafine WC1–x nanocrystals: an efficient cocatalyst for the significant enhancement of photocatalytic hydrogen evolution on g-C3N4.* The Journal of Physical Chemistry C, 2019. **123**(43): p. 26136-26144.
74. Zhang, Y., et al., *Single-atom Cu anchored catalysts for photocatalytic renewable H2 production with a quantum efficiency of 56%.* Nature Communications, 2022. **13**(1): p. 58.
75. Zhang, Y., et al., *Plasmonic copper nanowire@ TiO2 nanostructures for improving the performance of dye-sensitized solar cells.* Journal of Power Sources, 2017. **342**: p. 292-300.
76. Ahlawat, M., D. Mittal, and V. Govind Rao, *Plasmon-induced hot-hole generation and extraction at nano-heterointerfaces for photocatalysis.* Communications Materials, 2021. **2**(1): p. 1-15.
77. Chavez, S., U. Aslam, and S. Linic, *Design Principles for Directing Energy and Energetic Charge Flow in Multicomponent Plasmonic Nanostructures.* ACS Energy Letters, 2018. **3**(7): p. 1590-1596.
78. Dainton, F., I. Janovsky, and G. Salmon, *Evidence for the production of an oxidising radical on pulse-radiolysis of methanol.* Journal of the Chemical Society D: Chemical Communications, 1969(7): p. 335-336.
79. Yuan, Y. and Y. Iwasawa, *Performance and characterization of supported rhenium oxide catalysts for selective oxidation of methanol to methylal.* The Journal of Physical Chemistry B, 2002. **106**(17): p. 4441-4449.
80. Wang, W., R.-P. Ren, and Y.-K. Lv, *DFT study on the mechanism of methanol to methyl formate on the M@ C16B8 surface.* Materials Today Communications, 2021. **26**: p. 102090.
81. Li, S., et al., *Recent Advances in Plasmonic Nanostructures for Enhanced Photocatalysis and Electrocatalysis.* Advanced Materials, 2021. **33**(6): p. 2000086.
82. Yan, P., et al., *The regulation of reaction processes and rate-limiting steps for efficient photocatalytic CO2 reduction into methane over the tailored facets of TiO2.* Catalysis Science & Technology, 2019. **9**(6): p. 1451-1456.
83. Li, P., et al., *Crystal Facet-Dependent CO2 Photoreduction over Porous ZnO Nanocatalysts.* ACS Appl Mater Interfaces, 2020. **12**(50): p. 56039-56048.

84. Rao, V.G., U. Aslam, and S. Linic, *Chemical requirement for extracting energetic charge carriers from plasmonic metal nanoparticles to perform electron-transfer reactions.* Journal of the American Chemical Society, 2018. **141**(1): p. 643-647.
85. Chen, T., et al., *Plasmon-Driven Modulation of Reaction Pathways of Individual Pt-Modified Au Nanorods.* Nano letters, 2020. **20**(5): p. 3326-3330.
86. Kim, Y., J.G. Smith, and P.K. Jain, *Harvesting multiple electron–hole pairs generated through plasmonic excitation of Au nanoparticles.* Nature chemistry, 2018. **10**(7): p. 763-769.